Supporting Information

Direct measurement of the in-plane thermal diffusivity of semitransparent thin films by lock-in thermography: an extension of the slopes method

Alexandra Philipp[1], Nelson W. Pech-May[1**], Bernd A. F. Kopera[1], Anna M. Lechner[1], Sabine Rosenfeldt[1], Markus Retsch[1*]

[1]University of Bayreuth, Department of Chemistry, Universitaetsstr. 30, 95447 Bayreuth, Germany
[*]E-mail: markus.retsch@uni-bayreuth.de
**E-mail: nelson.pech@uni-bayreuth.de

Details of the analytical model for a semitransparent film are presented. Photographs of polymer samples, UV-vis and IR spectra of all samples as well as the influence of carbon coating, XRD and SAXS data, and reference thermal diffusivity measurements using XFA.

1) Modeling

Consider the geometry shown in Figure 1 of the main text. The power distribution $P(z)$ inside the semitransparent thin film can be calculated using the Beer-Lambert law taking into account multiple reflections of the laser beam at the film surfaces,[1]

$$P(z) = \frac{P_0(1-R)(e^{-\alpha z} + Re^{-2\alpha L}e^{\alpha z})}{1 - R^2 e^{-2\alpha L}}, \quad \text{(S1)}$$

where R is the reflectance and α is the absorption coefficient of the film, both taken at the laser wavelength. A fraction of this power is converted into heat $Q(z) = \chi P(z)$ and is the heating source of the film. Where χ is the efficiency of the light to heat conversion. We consider heat

conduction by diffusion in the film. Accordingly, the heat diffusion equation for the presented configuration reads

$$\nabla^2 T - \frac{i\omega}{D} T = -\frac{\chi P_0}{2K} \frac{e^{-\frac{2r^2}{a^2}}}{\pi a^2} \frac{(1-R)\alpha(e^{-\alpha z} - Re^{-2\alpha L} e^{\alpha z})}{(1-R^2 e^{-2\alpha L})}, \tag{S2}$$

where $T = T(\vec{r}, \omega)$ is the temperature field inside the sample at the angular frequency $\omega = 2\pi f$, D and K is the thermal diffusivity and thermal conductivity of the film, respectively. Because the film is thermally isotropic, Equation (S2) has cylindrical symmetry. Thus, we can express the temperature field as a Hankel transform:

$$T(r, z, \omega) = \int_0^\infty \delta J_0(\delta r) \left[A e^{\beta z} + B e^{-\beta z} + C e^{-\alpha z} + E e^{\alpha z} \right] d\delta, \tag{S3}$$

where δ is the Hankel space variable, $J_0(\cdot)$ is the Bessel function of zero order, $\beta^2 = \delta^2 + \frac{i\omega}{D}$ and the coefficients C and E are obtained from a particular solution of Equation (S2):[1]

$$C = \frac{\chi P_0}{2\pi K} \frac{(1-R)\alpha}{(\beta^2 - \alpha^2)} \frac{e^{-\frac{(\delta a)^2}{8}}}{1 - R^2 e^{-2\alpha L}}, \tag{S4a}$$

$$E = -\frac{\chi P_0}{2\pi K} \frac{(1-R)\alpha R e^{-2\alpha L}}{(\beta^2 - \alpha^2)} \frac{e^{-\frac{(\delta a)^2}{8}}}{1 - R^2 e^{-2\alpha L}}. \tag{S4b}$$

The solution of the homogeneous part of Equation (S2) gives the other two coefficients in Equation (S3) by considering the following boundary conditions:

$$K \left. \frac{dT}{dz} \right|_{z=0} = hT(z=0), \tag{S5a}$$

$$K \left. \frac{dT}{dz} \right|_{z=L} = -hT(z=L), \tag{S5b}$$

where h is the linearized combined coefficient of convective and radiative heat transfer.[2-3] Accordingly, the temperature field given in Equation (S3) can be written as

$$T(r, z, \omega) = \frac{\chi P_0}{2\pi K} \frac{(1-R)\alpha}{1 - R^2 e^{-2\alpha L}} \int_0^\infty \delta J_0(\delta r) \frac{e^{-\frac{(\delta a)^2}{8}}}{(\beta^2 - \alpha^2)} \left[\frac{A_0 e^{\beta z} + B_0 e^{-\beta z}}{E_0} + e^{-\alpha z} - R e^{-\alpha L} \left(\frac{A_1 e^{\beta z} + B_1 e^{-\beta z}}{E_0} + e^{\alpha z} \right) \right] d\delta. \tag{S6}$$

Where

$$A_0 = e^{-\beta L}(\beta - h')(\alpha + h') + e^{-\alpha L}(\beta + h')(-\alpha + h'), \quad \text{(S7a)}$$

$$B_0 = e^{\beta L}(\beta + h')(\alpha + h') + e^{-\alpha L}(\beta - h')(-\alpha + h'), \quad \text{(S7b)}$$

$$A_1 = e^{-\beta L}(\beta - h')(-\alpha + h') + e^{\alpha L}(\beta + h')(\alpha + h'), \quad \text{(S7c)}$$

$$B_1 = e^{\beta L}(\beta + h')(-\alpha + h') + e^{\alpha L}(\beta - h')(\alpha + h'), \quad \text{(S7d)}$$

$$E_0 = e^{-\beta L}(\beta - h')^2 - e^{\beta L}(\beta + h')^2, \quad \text{(S7e)}$$

and $h' = h/K$.

The semi-transparency of the film in the infrared (IR) region is also considered. In particular, for the detection range of our IR camera (7.5 – 14 μm), the signal is collected not only from the sample surface but also from the inside.

Let us consider an effective IR absorption coefficient γ, which averages the IR absorption over the detection range of our IR camera. This effective coefficient is a good approximation for materials with smoothly varying IR absorption spectra in the corresponding detection range.[4] Accordingly, the signal recorded by the IR camera can be written as,

$$S(r, z_0, \omega) = F \int_0^L \gamma e^{-\gamma|z - z_0|} T(r, z, \omega) dz, \quad \text{(S8)}$$

where $z_0 = \{0, L\}$ for the IR camera placed in the same side (front-face configuration) or in the backside (rear-face configuration) of the illuminated surface, respectively. The proportionality constant F includes the effect of the IR emissivity, sensor area, IR detection range and the derivative of the Planck distribution at room temperature.

Setting $z_0 = 0$ in Equation (S8) allows us to evaluate the resulting integral and obtain an expression for the signal recorded by the IR camera, in the front-face configuration (see Equation (1) in main text). Similarly, to the previous case, we set $z_0 = L$ and evaluate the integral in Equation (S8). We obtain the following expression for the signal recorded by the IR camera, in the rear-face configuration (see Equation (2) in the main text).

In order to show the equivalence of front-face and rear-face signals for the thermally thin case, we performed simulations using Equations (1) and (2) of the main text and we plot the difference in 'amplitude' and phase. The results are shown in Figures S1a and S1b, respectively. For these simulations, we have used the same parameters as in Figure 2a of the main text.

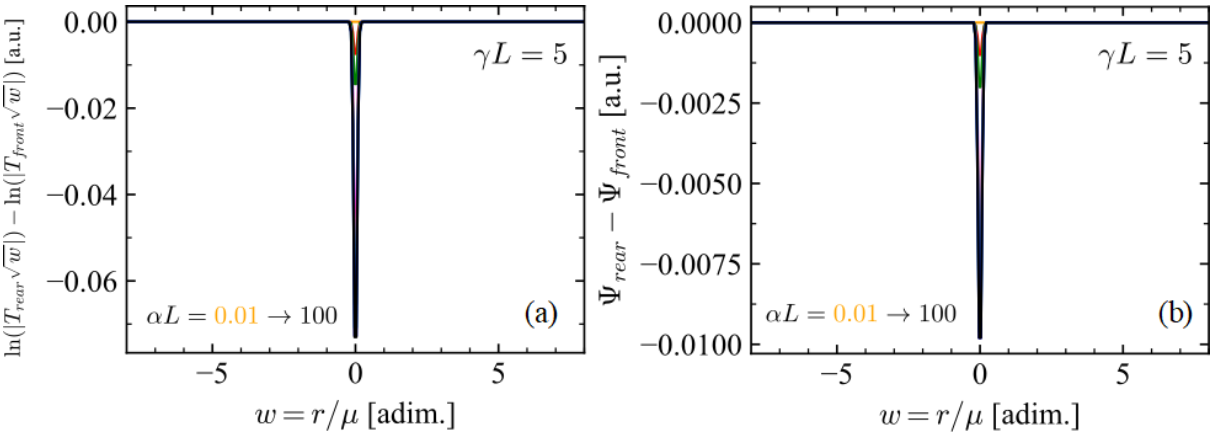

Figure S1. Difference in (a) amplitude and (b) phase between the surface temperature at $z = L$ (rear-face) and the front surface temperature at $z = 0$. Note that differences appear only near to the excitation spot, but for $|r| \gtrsim \mu$ both temperatures are equal.

To validate our simulations in Chapter 3.1, for a wide range of both absorption coefficients, we perform simulations at three different values of the IR absorption coefficient ($\gamma L = 0.10, 5$ and 50). For each case, the optical absorption coefficient to the exciting wavelength was varied over a wide range: $0.01 \leq \alpha L \leq 100$. The product between the amplitude derivative and phase derivative is depicted in S2a-c. Note that for $|r| \geq \mu$, the product of the derivatives is constant, independent of the optical absorption at the exciting wavelength and for each of the three different values of γL. This is analogous to the product of the slopes $m_{\ln(|T\sqrt{r}|)} \cdot m_{\Psi} = \pi f/D$ for the optically opaque case.[5] Actually, the optically opaque case is covered in our simulations, as represented in S2c for large values of αL.

S2d-f show the product of derivatives for three different values of the optical absorption to the exciting wavelength ($\alpha L = 0.10, 5$ and 50), covering a wide range of IR absorption coefficients $0.01 \leq \gamma L \leq 100$. Once again, for $|r| \geq \mu$, the product of the derivatives is constant, independent of the IR optical absorption and for each of the three different values of αL. The optically opaque case is covered in S2f for large values of γL.

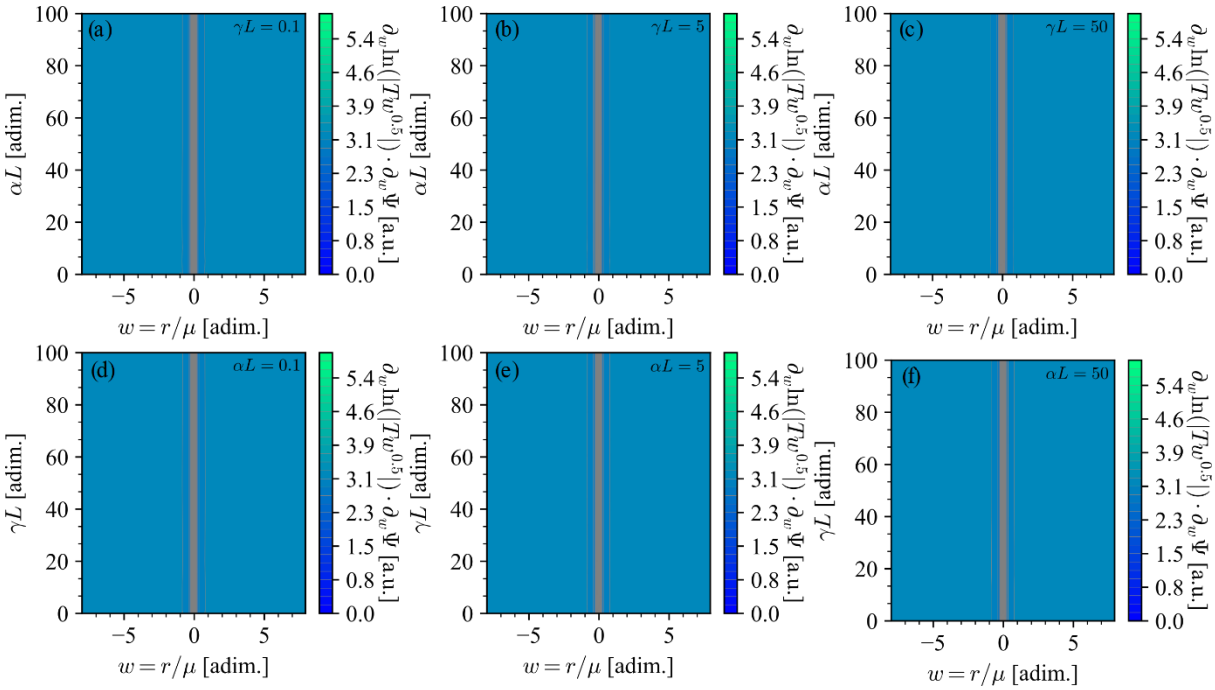

Figure S2. Product between amplitude and phase derivatives. Upper row (a)-(c): three different values of the IR absorption coefficient ($\gamma L = 0.10, 5$ and 50), covering a wide range of optical absorption coefficients to the exciting wavelength $0.01 \leq \alpha L \leq 100$. Lower row (d)-(f): three different values of the optical absorption to the exciting wavelength ($\alpha L = 0.10, 5$ and 50), covering a wide range of IR absorption coefficients $0.01 \leq \gamma L \leq 100$.

2) Experimental section

Photographs of PMMA and LDPE samples for LIT measurements

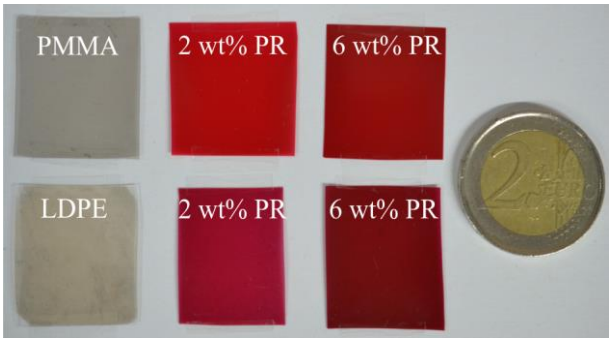

Figure S3. Photographs of LIT samples. Upper row: PMMA film with 20 nm carbon, PMMA film with 2 and 6 wt% PR, respectively. Lower row: LDPE film with 20 nm carbon, LDPE film 2 and 6 wt% PR, respectively.

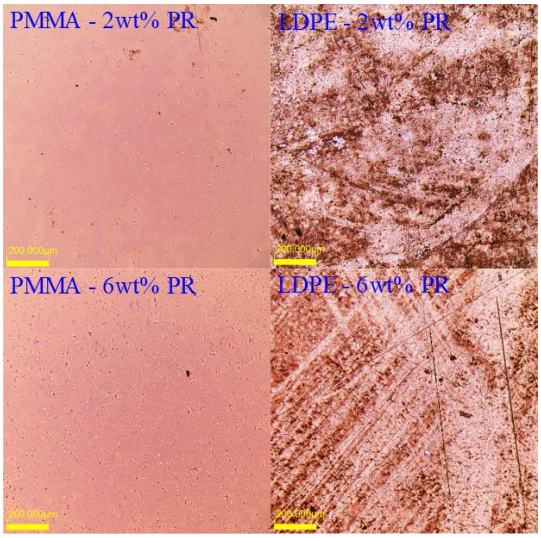

Figure S4. Micrographs of LIT samples with PR. Upper row: PMMA and LDPE films with 2 wt% PR. Lower row: PMMA and LDPE films with 6 wt% PR.

Lock-in thermography set-up

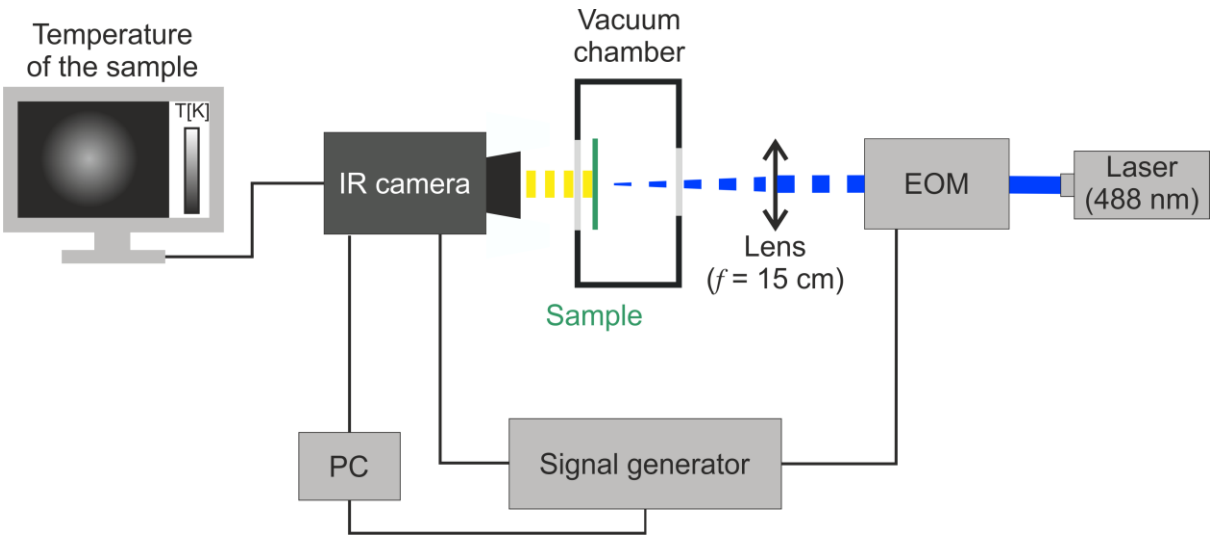

Figure S5. Schematic set-up used for lock-in thermography measurements. PC and EOM stand for personal computer and electro optic modulator, respectively.

IR and UV-vis spectra of PMMA and LDPE samples for LIT measurements

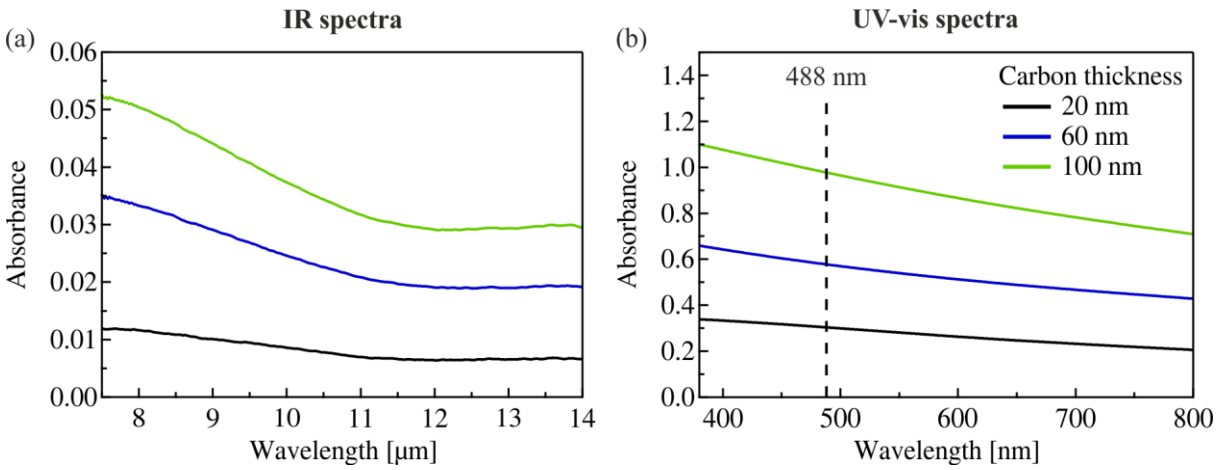

Figure S6. Influence of carbon coating on the optical properties: (a) IR spectra and (b) UV-vis spectra of 20 nm, 60 nm, and 100 nm carbon (The spectra are represented relative to an uncoated KBr disc as control). The dashed line at 488 nm marks the wavelength of the incident laser used in lock-in measurements. The absorbance of IR and UV-vis light increases with an increasing carbon layer. The coating leads to a higher absorbance of light in the UV-vis range compared to IR light.

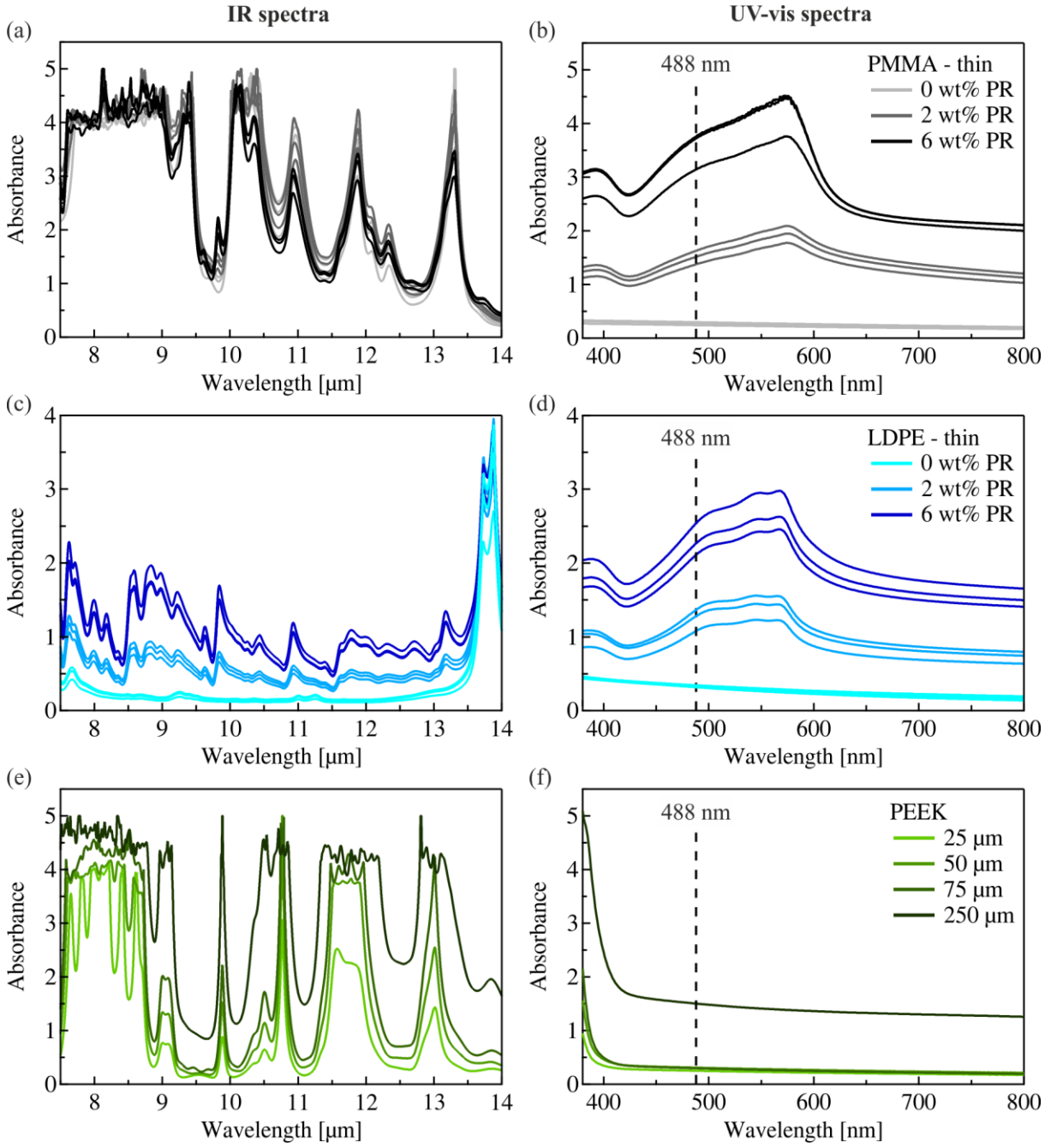

Figure S7. Optical properties of the thin, free-standing polymeric films measured with lock-in thermography. (a) IR spectra and (b) UV-vis spectra of PMMA films with 0 wt%, 2 wt%, and 6 wt% PR, respectively. (c) IR spectra and (c) UV-vis spectra of LDPE films with 0 wt%, 2 wt%, and 6 wt% PR, respectively. (d) IR spectra and (e) UV-vis spectra of a 25 μm, 50 μm, 75 μm, and 250 μm PEEK film, respectively. The dashed line at 488 nm marks the wavelength of the incident laser used in lock-in measurements. Absorbance values higher than 4 units are difficult to resolve accurately with our detector. Therefore, we set the opaqueness threshold to $A_{Vis}>4$ (for the excitation wavelength) and $A_{IR}>4$ (in the IR range).

Reference thermal diffusivity measurements of thick PMMA and LDPE samples

1) ***Preparation of thick reference samples for Xenon flash analysis***

1 mm thick PMMA samples were fabricated by compounding and injection molding. PMMA pellets and PR powder were mixed under N_2 flow in a twin-screw compounder with a stirring speed of 40 rpm and at a temperature of 240 °C. Then, the compounded material was directly filled into the injection unit. Disks with a diameter of ∼27 mm and a thickness of ∼1 mm were fabricated using an injection force of 6 kN and a tool temperature of 20 °C. In this way, PMMA disks with 0 wt%, 2 wt%, and 6 wt% PR, respectively, were prepared. LDPE samples were taken from the remaining LDPE disks which were already prepared using injection molding (see Experimental section in the main text).

2) ***Cross-plane thermal diffusivity measurements using Xenon flash analysis (XFA)***

Xenon flash analysis (XFA) was used to obtain reference thermal diffusivity values for the fabricated PMMA and LDPE samples. We performed cross-plane thermal diffusivity measurements on an XFA500 Xenon flash apparatus (Linseis), equipped with an InSb infrared (IR) detector. The upper and lower sample surfaces were coated with a thin graphitic layer (each ∼10 µm). Since the thickness of the coating is significantly thinner than the sample thickness (20 µm ≪ 1000 µm), it does not affect the measurement result. The coating ensures a good absorbance of the Xenon flash and a high IR emissivity. The sample thickness which is needed to obtain the thermal diffusivity was measured with a Litematic VL-50 (Mitutoyo). All XFA measurements were performed in air at room temperature (295 K). The LDPE samples were measured before and after thermal annealing (90 °C, one week).

3) ***X-ray diffraction (XRD) and small angle X-ray scattering (SAXS)***

To demonstrate the amorphous nature of the PMMA samples and the semi-crystallinity of the LDPE samples we performed X-ray diffraction (XRD). The measurements were conducted in Bragg-Brentano geometry on an Empyrean system with a PIXEL solid-state detector (PANalytical, Almelo, Netherlands) using Cu-radiation.

Small-angle X-ray scattering (SAXS) was performed on the PMMA and LDPE samples using the lab-based system Ganesha Air (SAXSLAB, Denmark), equipped with a rotating anode (copper, MicroMax 007HF, Rigaku Corporation, Japan) and a position sensitive detector (Pilatus 300K, Dectris). The samples (and air as background) were measured as obtained in parallel and perpendicular beam geometry. Different detector positions were used to cover a larger scattering range q ($q = \frac{4\pi}{\lambda}\sin\left(\frac{2\theta}{2}\right)$).

4) ***Discussion of polymer microstructure***

The pure PMMA samples show broad oscillations without prominent Bragg reflections in the XRD regime proving their amorphous nature (Figure S8, black curve). The broad oscillations around 13.5 °, 30 ° and 42 ° result from the packing and defined backbone sequence of the polymeric chains. These characteristic patterns are also obtained for the dye-doped PMMA samples (Figure S8, red curve, and Figure S9a, b), which additionally show small reflections due to tiny crystallites of phenol red. The combination of XRD and SAXS of a pure PMMA sample (Figure S8, inset) indicates a rough surface of the films ($I(q) \propto q^{-2.8}$). In that context, one may imagine the texture of the sample area as a dense fractal-like object.

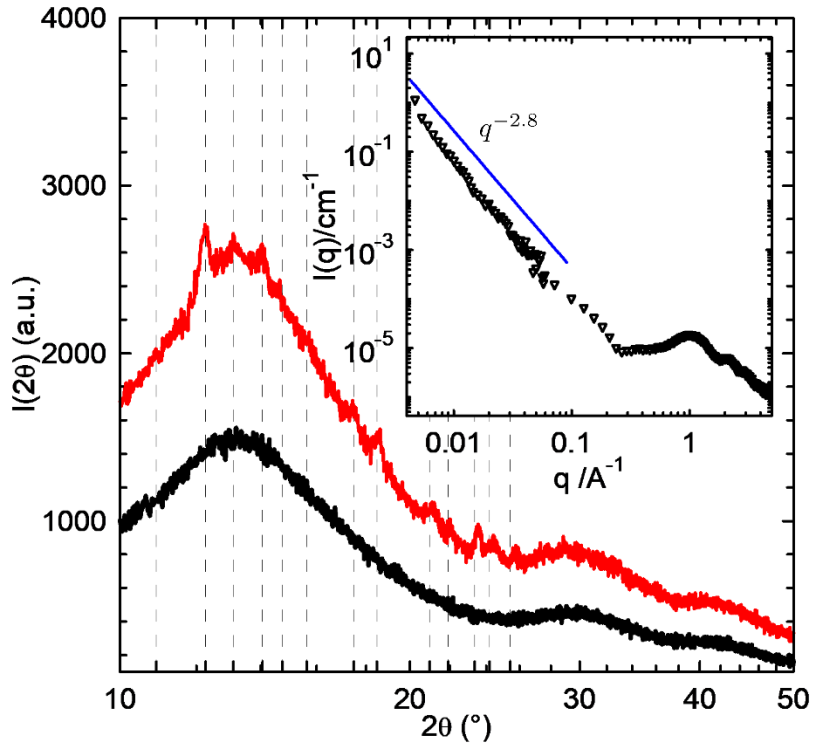

Figure S8. XRD pattern of thick PMMA samples without PR (black line) and with 6 wt% PR (red line) as well as the expected pattern of phenol red (gray vertical dashed lines). The inset shows the X-ray intensity of the pure PMMA sample over a wider *q* range (triangles, SAXS and XRD) and a theoretical intensity calculated for a mass fractal (blue line).

As can be seen in Figure S9a and b, the XRD patterns reveal no significant differences in the polymeric structure between the thin and thick PMMA samples prepared for lock-in thermography and Xenon flash analysis, respectively. In both cases, the small Bragg reflections base on the incorporated PR dye and increase slightly with increasing concentration of the dye. This shows that all samples exhibit a similar polymeric microstructure independent of the PR content, sample thickness, and preparation method (injection molding *vs.* doctor-blading).

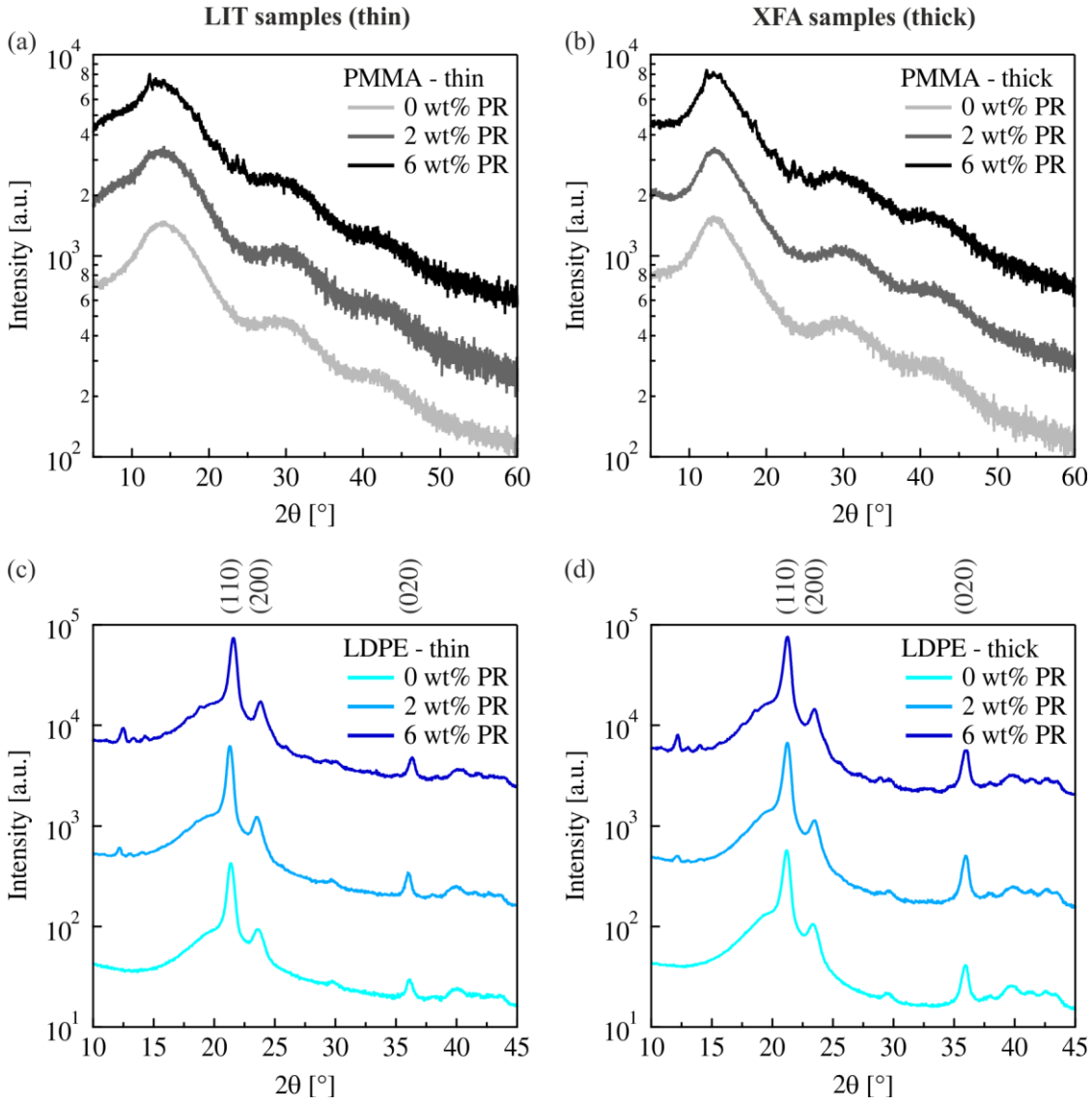

Figure S9. XRD curves of amorphous PMMA and semi-crystalline LDPE: (a) thin PMMA used for lock-in thermography (LIT) measurements, and (b) thick PMMA for Xenon flash analysis (XFA), (c) thin LDPE for LIT measurements, and (d) thick LDPE for XFA. Curves are presented with a vertical shift.

LDPE is a low-density, semi-crystalline polymer. The semi-crystallinity of the LDPE films is visible by the pronounced Bragg reflexes at 21.2 °(100 % peak), 23.3 ° and 36.0 ° (Figure S9c and d). The reflections correspond to [110], [200], and [020] of space group Pnam. As expected, the PR doped films show additionally small Bragg spots due to the dye.

We found comparable degrees of crystallinity (~ 45%) for all LDPE samples. Consequently, the addition of phenol red does not affect the degree of crystallinity of the LDPE samples.

Furthermore, also the subsequent hot-pressing of the injection molded LDPE disks does not change the degree of crystallinity.

Usually, one expects for a semi-crystalline film that (i) the amorphous and crystalline regions are randomly distributed over the solid material (isotropy) and that (ii) the small crystallites are polydisperse. Nevertheless, due to external forces like shear stress or elevated temperatures phase segregation between the amorphous phase and the crystallites cannot be ruled out.

Consequently, we performed SAXS experiments in parallel and perpendicular beam geometries to study the in-plane and cross-plane polymeric microstructures, respectively. Figure S10 shows an example of such a study for the LDPE samples with 6 wt% PR. Astonishing, the SAXS patterns taken perpendicular exhibit a broad reflection at $q \approx 0.04$ Å^{-1}, which corresponds to a correlation length of about 15 nm and hints to a two-phase LDPE system (segregation of crystallites and amorphous LDPE). This feature is anisotropic spot-like for the thick sample (Figure S10a) and isotropic for the thin film (Figure S10b). As a consequence, the crystallites of the thick samples have a stronger tendency to align lamellar-like parallel to the sample surface (i.e., in in-plane direction) compared to the thin samples.

In the mesoscopic scattering signals observed for the thick and thin samples in parallel beam geometry (Figure S10c and S10d), the oscillation at $q \approx 0.04$ Å^{-1} is attenuated, and the patterns appear more isotropic.

Thus, the thick samples (prepared for XFA) and thin films (prepared for LIT) exhibit a different microstructure despite their comparable degree of crystallinity. Both samples show a preferred orientation of the crystallites in the in-plane direction and more random orientation in the cross-plane direction. However, the anisotropy is much more pronounced for the thick samples. This difference in the microstructure may be associated with the different fabrication processes and the applied temperature gradients (injection molding *vs.* injection molding and subsequent hot-pressing).

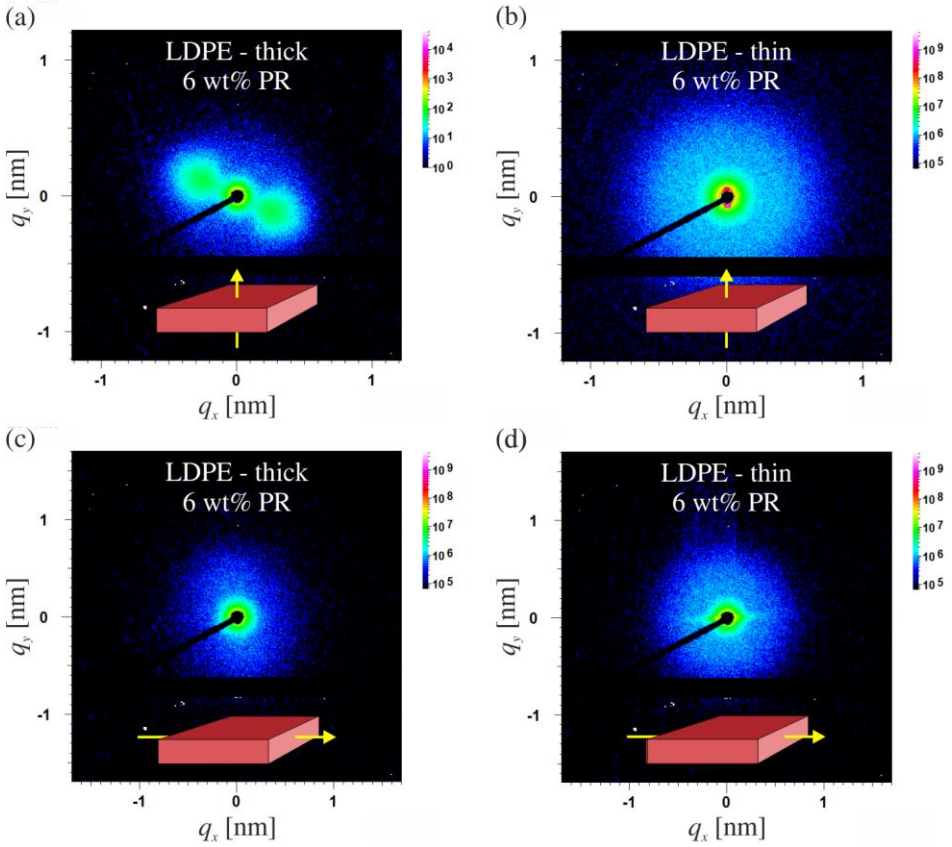

Figure S10. 2D SAXS patterns of LDPE films with 6 wt% PR in perpendicular (a, b) and parallel (c, d) beam geometry (see sketch: sample with beam direction).

In Figure S11 the two-dimensional SAXS data of a thick LDPE sample as used for XFA and after additional annealing at 90 °C for one week are compared to illuminate the effect of the temperature/fabrication method on the orientation of the crystallites. All annealed samples show a significantly more preferred orientation of the crystallites compared to the non-annealed state. Note, that the spots appear even triangular for the data of the annealed film in perpendicular geometry and at the same time, the amorphous halo is less pronounced. We conclude that a direction dependent crystal growth is introduced by thermal annealing. The same trend is observed in case of the thin films, but much less pronounced.

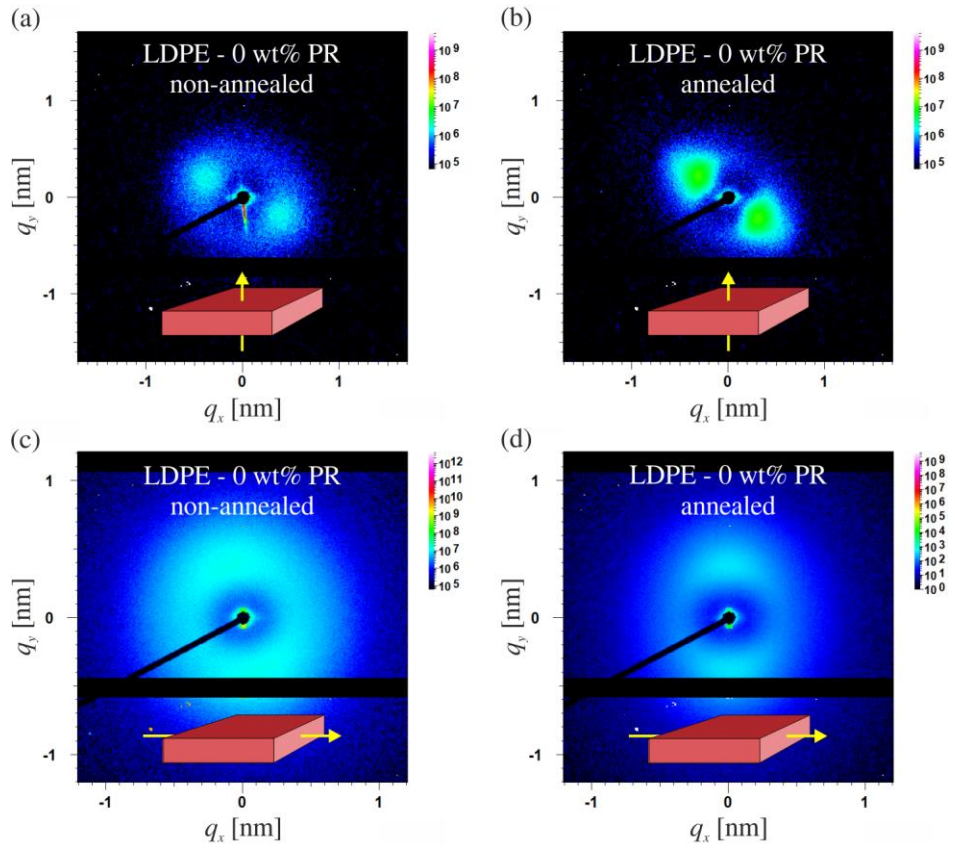

Figure S11. 2D SAXS patterns of thick LDPE samples (for XFA) with 0 wt% PR in perpendicular (a, b) and parallel (c, d) beam geometry (see sketch: sample with beam direction).

5) *Comparison of thermal diffusivity data (LIT vs. XFA)*

Figure S12 summarizes the thermal diffusivity values obtained for the fabricated PMMA and LDPE samples with 0, 2, and 6 wt% PR, respectively. The *in-plane* thermal diffusivity of the thin, free-standing samples was determined using lock-in thermography (LIT). The 1 mm thick reference samples were characterized using Xenon flash analysis (XFA). It is to be noted that this measurement technique gives the *cross-plane* thermal diffusivity.

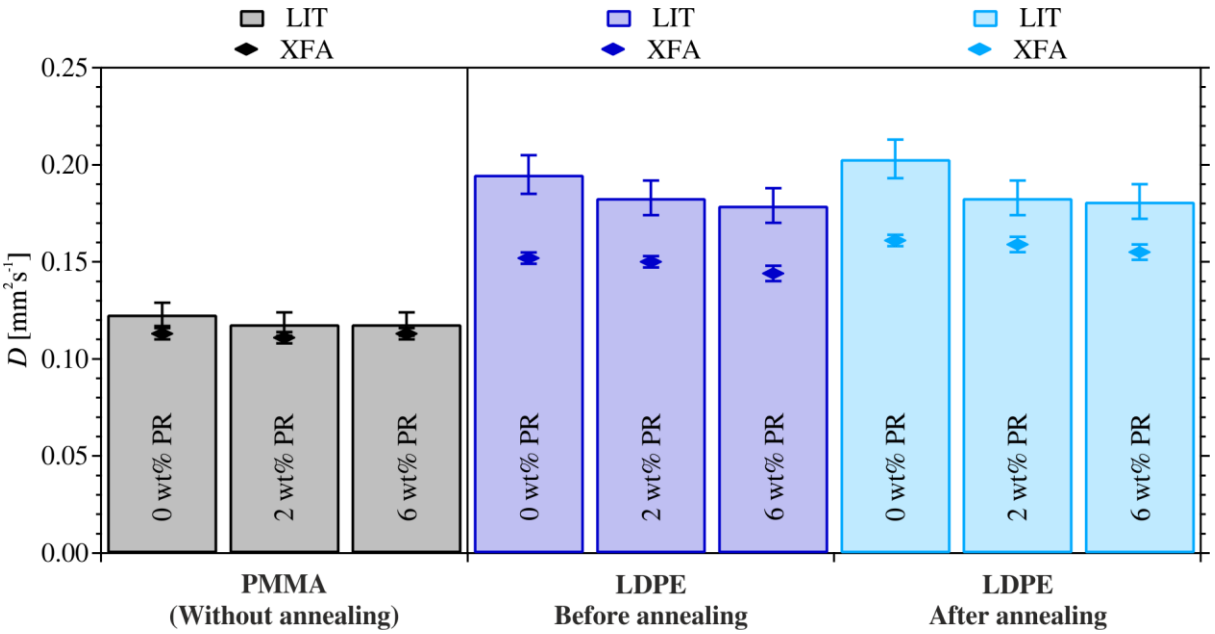

Figure S12. Thermal diffusivity *D* of PMMA and LDPE with 0, 2, and 6 wt% phenol red (PR), respectively. The thin samples (~ 200 µm) were measured with lock-in thermography ((LIT), bars) that determines the *in-plane* thermal diffusivity; the thick samples (~ 1 mm) were analyzed with Xenon flash analysis ((XFA), markers) that gives the *cross-plane* thermal diffusivity. LDPE samples were measured before and after thermal annealing (90 °C, one week). The error bars arise from 5 % uncertainty (LIT) and from the standard deviation of the averaged value (XFA). Two to three samples were measured in each case.

As discussed in the main text, we obtain an in-plane thermal diffusivity of ~ 0.12 mm^2s^{-1} for all PMMA samples independent of the PR content. The cross-plane values obtained from XFA are ~ 0.11 mm^2s^{-1}, and thus close to the data obtained from LIT. This good agreement confirms that the microstructure of the amorphous polymer is similar (see XRD curves in Figure S8, Figure S9a and S9b) leading to isotropic thermal diffusivity values.

However, in the case of LDPE (before annealing), we extracted significantly lower cross-plane thermal diffusivities from XFA (~ 20 %). We relate this discrepancy to the difference in the underlying microstructure as discussed above. Since the degree of crystallinity of all samples is the same, the preferred in-plane orientation leads apparently to a reduced cross-plane thermal diffusivity as measured by XFA.

Thermal annealing at 90 °C for one week led to a more pronounced anisotropy within the thick films. In comparison to the values before thermal annealing, we obtained similar in-plane

thermal diffusivity values from LIT and slightly higher cross-plane thermal diffusivity values from XFA after annealing.

In summary, we found that comparable in-plane and cross-plane thermal diffusivity values are obtained for an amorphous polymer independent of the fabrication method. In case of a semi-crystalline polymer, the fabrication method has a strong influence on the polymer microstructure, and thus on the in-plane and cross-plane thermal diffusivity, which renders a quantitative comparison difficult.

References

1. Pech-May, N. W.; Mendioroz, A.; Salazar, A., Simultaneous measurement of the in-plane and in-depth thermal diffusivity of solids using pulsed infrared thermography with focused illumination. *NDT&E Int.* **2016,** *77*, 28-34.

2. Kanstad, S. O.; Nordal, P.-E., Experimental aspects of photothermal radiometry. *Can. J. Phys.* **1986,** *64* (9), 1155-1164.

3. Salazar, A.; Mendioroz, A.; Fuente, R., The strong influence of heat losses on the accurate measurement of thermal diffusivity using lock-in thermography. *Appl. Phys. Lett.* **2009,** *95* (12).

4. Walther, H. G.; Seidel, U.; Karpen, W.; Busse, G., Application of modulated photothermal radiometry to infrared transparent samples. *Rev. Sci. Instrum.* **1992,** *63* (11), 5479-5480.

5. Mendioroz, A.; Fuente-Dacal, R.; Apinaniz, E.; Salazar, A., Thermal diffusivity measurements of thin plates and filaments using lock-in thermography. *Rev. Sci. Instrum.* **2009,** *80* (7), 074904.